REPORT DOCUMENTATION PAGE

1. REPORT DATE (DD-MM-YYYY)	2. REPORT TYPE	3. DATES COVERED (From - To)
05-02-2013	Journal Article	

4. TITLE AND SUBTITLE	5a. CONTRACT NUMBER
Optical Algorithm for Cloud Shadow Detection Over Water	
	5b. GRANT NUMBER
	5c. PROGRAM ELEMENT NUMBER
	0602345N

6. AUTHOR(S)	5d. PROJECT NUMBER
Ruhul Amin, Richard Gould, Weilin Hou, Robert Arnone and Zhongping Lee	
	5e. TASK NUMBER
	5f. WORK UNIT NUMBER
	73-6287-A1-5

7. PERFORMING ORGANIZATION NAME(S) AND ADDRESS(ES)	B. PERFORMING ORGANIZATION REPORT NUMBER
Naval Research Laboratory Oceanography Division Stennis Space Center, MS 39529-5004	NRL/JA/7330--11-0578

9. SPONSORING/MONITORING AGENCY NAME(S) AND ADDRESS(ES)	10. SPONSOR/MONITOR'S ACRONYM(S)
Office of Naval Research One Liberty Center 875 North Randolph Street, Suite 1425 Arlington, VA 22203-1995	ONR
	11. SPONSOR/MONITOR'S REPORT NUMBER(S)

12. DISTRIBUTION/AVAILABILITY STATEMENT

Approved for public release, distribution is unlimited.

20130422095

13. SUPPLEMENTARY NOTES

14. ABSTRACT

The application of ocean color product retrieval algorithms for pixels containing cloud shadows leads to erroneous results. Thus, shadows are an important scene type that should be Identified and excluded from the set of clear-sky pixels. In this paper, we present an optical cloud shadow-detection technique called the Cloud Shadow Detection Index (CSDI). This approach is for homogeneous water bodies such as deep waters where shadow detection Is very challenging due to the relatively small differences In the brightness values of the shadows and neighboring sunlit or some other regions. The CSDI technique is developed based on the small differences between the total radiances reaching the sensor from the shadowed and neighboring sunlit regions of similar optical properties by amplifying the differences through Integrating the spectra of the two regions. The Integrated Value (IV) is then normalized by the mean of the IVs within a spatial adaptive sliding box where atmospheric and marine optical properties are assumed homogeneous. Assuming that the true color and the IV images represent accurate shadow locations, the results were visually compared. The CSDI images agree reasonably well with the corresponding true color and the IV images over open ocean. Also, the shape of the cloud shadow particularly for the Isolated cloud closely follows that of the cloud, as expected, reconfirming the potential of the CSDI technique.

15. SUBJECT TERMS

Hyperspectral Imagery, ocean color, optical algorithm, remote sensing, shadow detection

16. SECURITY CLASSIFICATION OF:			17. LIMITATION OF ABSTRACT	18. NUMBER OF PAGES	19a. NAME OF RESPONSIBLE PERSON
a. REPORT	b. ABSTRACT	c. THIS PAGE	UU	10	Ruhul Amin
Unclassified	Unclassified	Unclassified			19b. TELEPHONE NUMBER (Include area code) 228-688-5000

Optical Algorithm for Cloud Shadow Detection Over Water

Ruhul Amin, Richard Gould, Weilin Hou, Robert Arnone, and Zhongping Lee

Abstract—The application of ocean color product retrieval algorithms for pixels containing cloud shadows leads to erroneous results. Thus, shadows are an important scene type that should be identified and excluded from the set of clear-sky pixels. In this paper, we present an optical cloud shadow-detection technique called the Cloud Shadow Detection Index (CSDI). This approach is for homogeneous water bodies such as deep waters where shadow detection is very challenging due to the relatively small differences in the brightness values of the shadows and neighboring sunlit or some other regions. The CSDI technique is developed based on the small differences between the total radiances reaching the sensor from the shadowed and neighboring sunlit regions of similar optical properties by amplifying the differences through integrating the spectra of the two regions. The Integrated Value (IV) is then normalized by the mean of the IVs within a spatial adaptive sliding box where atmospheric and marine optical properties are assumed homogeneous. Assuming that the true color and the IV images represent accurate shadow locations, the results were visually compared. The CSDI images agree reasonably well with the corresponding true color and the IV images over open ocean. Also, the shape of the cloud shadow particularly for the isolated cloud closely follows that of the cloud, as expected, reconfirming the potential of the CSDI technique.

Index Terms—Hyperspectral imagery, ocean color, optical algorithm, remote sensing, shadow detection.

I. Introduction

S PECTRAL information collected by optical satellite sensors can provide important information for various global remote sensing applications. However, clouds cause a serious problem for these sensors, particularly over humid tropical regions. Throughout the year, about two-thirds of the Earth's surface is always covered by clouds [1]. The problem for the optical sensor is that clouds not only conceal the ground but also cast shadows, and these shadows also occur in the observed images along with the clouds. Unlike airborne imaging where shadows can be minimized by flying at certain times during

the day, low-Earth-orbit satellite-based sensors are limited to acquiring images at fixed times of the day. If the solar elevation is low at the time, then the presence of shadow will be unavoidable. The main problem caused by shadows is either a reduction or total loss of information in an image [2]. Since ocean color algorithms are developed for water pixels illuminated by both direct solar irradiance and sky light, the radiance values in shadow pixels lead to the corruption of biophysical parameters derived from those pixels. Cloud shadow can produce errors of 30%–40% in the observed reflectance from the affected pixels over lands [3]. Similar errors can be expected over waters as well, although such studies have never been conducted. Since ocean color products are retrieved based on the assumption that the remote sensing reflectances are accurate, a small inaccuracy in the reflectance can lead to significant errors in the retrieved products. In particular, since most of the product retrieval algorithms are band ratio algorithms, a small disproportionate alteration in the spectral reflectance amplitude can change the band ratios considerably and, hence, the retrieved products [4], [5]. However, cloud shadow detection in ocean color scene can be important and beneficial. For example, the cloud shadowed pixel (pixel illuminated by only skylight photons since direct photons are removed by the cloud) in combination with the neighboring sunlit pixel (pixel illuminated by both direct solar and skylight photons) of similar optical properties can be used to remove atmospheric effects from these scenes [6]–[8]. The neighboring sunlit pixel then can be used as known reflectance targets for validation of the sensor calibration and atmospheric corrections [6], [8]. Cloud shadow is important for many other reasons as well. For example, cloud shadow can impact mesoscale atmospheric circulations that lead to major convective storm systems [9], [10]. Furthermore, cloud shadow can also be used to estimate both cloud base [11], [12] and cloud-top height [13] which are still a challenge to estimate reliably from space [14].

There are numerous algorithms for cloud detection [14]–[24]. However, relatively few cloud shadow-detection algorithms [23]–[30] have appeared in the literature even though accurate detection of cloud shadow is important for many atmospheric and terrestrial applications [3], [9], [10]. Most of the shadow detection techniques described in the literature deal with shadows over land [3], [23]–[29]. Few attempts have been made to detect shadows specifically over water [16], [31], while shadow detection over water is becoming significant as the spatial resolutions of the ocean color sensors are getting finer. This is because the small-scale shadow features appear in the acquired images.

R. Amin, R. Gould, W. Hou, and R. Arnone are with Code 7333, U.S. Naval Research Laboratory, Stennis Space Center, MS 39529 USA (e-mail: ruhul.amin@nrlssc.navy.mil; gould@nrlssc.navy.mil; wilin.hou@nrlssc.navy.mil; arnone@nrlssc.navy.mil).

Z. Lee is with the Department of Environmental, Earth and Ocean Sciences, University of Massachusetts, Boston, MA 02125 USA (e-mail: zhongping.lee@umb.edu).

The locations of shadows in the image depend on cloud elevation and the incidence angle of the sunlight at that time. The cloud shadow location can be determined by the means of geometrical calculations if the spatial location of cloud, i.e., cloud-top and cloud-bottom heights, and the sun and satellite positions are known. However, geometry-based approaches [25], [26] have challenging issues besides requiring too much CPU to run operationally [16], [31]. The main issue for geometry-based approach is the estimation of cloud vertical height which is required to determine the relative shadow location. Normally, thermal channels can be used to estimate the cloud-top height [15]. However, it is still a challenge to determine the cloud-bottom height without cloud profiling measurements [32]. The solar reflective bands cannot provide information about the cloud-top height, and the cloud-bottom information cannot be reliably estimated from passive solar–thermal data either [33]. To determine accurate shadow location, both heights are important particularly for isolated clouds. In any event, many ocean color sensors such as the Sea-viewing Wide Field-of-view Sensor do not have necessary channels to estimate cloud vertical heights. Therefore, in order to identify the shadow locations from these sensors, we need an algorithm that uses visible channels since these channels are always present on the ocean color sensors.

It can be easy to identify the cloud regions simply by using brightness thresholds, but it is difficult to identify the shadow regions this way because their brightness values can be very close to those of their neighbors or some other regions. Distinguishing shadows over water bodies based on spectral reflectance shape and amplitude information is also very difficult or possibly even impossible [34]. Shadows over water pixels do not have any specific spectral features while the brightness varies with atmospheric conditions and imaging geometry. Therefore, the brightness or the spectral shape alone may not be appropriate for shadow detection. However, brightness values from shadow and close-by sunlit regions over water can provide a great deal of information if a small portion of the image (where optical properties of water and atmosphere are uniform) is examined at a time. This is because the water-leaving radiance over sunlit pixels results from both direct and diffuse solar irradiance, while the water-leaving radiance over shadowed pixels results from only diffuse solar irradiance. The path radiance from the shadowed pixel to the sensor is also slightly lower, depending on how much of the atmospheric path radiance is shadowed. Therefore, the total radiance at the top of the atmosphere measured over the shadowed pixels is slightly lower compared to the adjacent sunlit pixels. Assuming that the optical properties of water and atmosphere are homogeneous around shadowed and adjacent sunlit regions, examining the radiance difference among these small uniform regions together enables us to separate the shadowed regions.

In this paper, we propose a cloud shadow-detection technique for optical imageries acquired over water by satellite/airborne sensors. This technique does not require any angular information (viewing or solar) or any estimation of cloud vertical heights. It is entirely based on measurements in the optical channels. To our knowledge, it is the first optical cloud shadow-detection technique over water.

II. DATA

The Hyperspectral Imager for the Coastal Ocean (HICO) has been operating aboard the International Space Station (ISS) since installation on September 24, 2009 [35], [36]. HICO provides hyperspectral images at 100-m resolution optimized for the coastal ocean. It collects radiance at 128 contiguous spectral channels from 350–1070-nm range. However, it is most sensitive in the spectral wavelengths ranging from 400 to 900 nm, which are the most utilized spectral region for ocean color studies. Each HICO scene is roughly 50 km in width by 200 km in length. The HICO data flow from the ISS provides a maximum of 15 scenes per day, and the sensor is managed by the U.S. Naval Research Laboratory.

Since shadow detection becomes significant for high-spatial-resolution images due to the imaging of small-scale shadows, we test our technique using the HICO data acquired over various regions around the globe. HICO also has higher spectral resolution. Thus, the contrast between shadowed and adjacent sunlit regions would be higher after integrating the spectra, which is advantageous for the shadow detection. The Cloud Shadow Detection Index (CSDI) technique should also work for multispectral data. However, it still needs to be tested using relatively high spatial resolution multispectral data.

III. BACKGROUND

Let us assume that solar elevation is relatively low and the sensor is at nadir; a small compact thick cloud over water prevents direct solar photons from impinging on the sea surface and shadows a region. The water-leaving radiance from the shadowed region $L_w^{sdw}(\lambda)$ that reaches the sensor results from only skylight photons since direct photons are removed by the cloud. An adjacent patch of water from a sunlit region has identical inherent optical properties to those of the shadowed region. Refer water-leaving radiance from the neighboring sunlit region as $L_w^{sny}(\lambda)$, which results from the illuminations of both direct solar and skylight photons.

The atmosphere is also assumed to be homogeneous in shadow and neighboring sunlit regions as they are adjacent. Let L_a represent the contribution from the atmosphere (path radiance due to light scattering by air molecules and aerosol particles) and sea-surface reflectance [7]. The total radiance measured at the sensor's altitude from the sunlit area can be expressed as

$$L_t^{sny}(\lambda) = L_a(\lambda) + t(\lambda)L_w^{sny}(\lambda) \qquad (1)$$

where $t(\lambda)$ represents the diffuse transmittance of the atmosphere for the water-leaving radiance.

The total radiance measured at the sensor's altitude over the shadowed region can be expressed similarly with some differences in the path radiance and diffuse transmittance expected. The path radiance from the shadowed region should be lower, since part of the viewing path to the shadowed region is also shadowed. Therefore, it should produce less path radiance, depending on how much of the atmosphere is shadowed [8]. The apparent path transmittance of the water-leaving radiance from the shadowed region may be slightly higher since the adjacent areas of the scene are generally brighter, so the

apparent transmittance of the viewing path to the shadow will be enhanced by photons reflected from the bright portion of the image and scattered into the field of view of the sensor [8].

The total radiance measured over the shadowed region can be expressed as

$$L_t^{sdw}(\lambda) = L_a(\lambda) - \Delta L_a(\lambda) + (t(\lambda) + \Delta t(\lambda)) L_w^{sdw}(\lambda). \quad (2)$$

The Δ term represents the perturbations due to the differences in illuminations between the sunlit and shadowed regions.

The water-leaving radiance can be expressed as two parts: one part caused by the backscattering of the diffuse skylight and the other part caused by the backscattering of the direct solar beam. For the sunlit and shadowed regions, the water-leaving radiance can be expressed as $L_w^{sny}(\lambda) = L_{w^{sky}}^{sny}(\lambda) + L_{w^{dir}}^{sny}(\lambda)$ and $L_w^{sdw}(\lambda) = L_{w^{sky}}^{sdw}(\lambda)$, respectively, since $L_{w^{dir}}^{sdw}(\lambda) = 0$, where $L_{w^{sky}}^{sny}(\lambda)$ and $L_{w^{dir}}^{sny}(\lambda)$ represent the water-leaving radiances caused by diffuse skylight and direct solar beam in the sunlit region, respectively. $L_{w^{sky}}^{sdw}(\lambda)$ and $L_{w^{dir}}^{sdw}(\lambda)$ represent the water-leaving radiances caused by diffuse skylight and direct solar beam in the shadowed region, respectively.

The diffuse irradiance incident on the shadow area and that incident on the close-by sunlit area are unequal because scattering from cloud may increase the diffuse irradiance incident on the neighboring sunlit region [8]. According to [8], $L_{w^{sky}}^{sny}(\lambda)$ can be expressed as $L_{w^{sky}}^{sny}(\lambda) = L_{w^{sky}}^{sdw}(\lambda) + \Delta L_{w^{sky}}^{sdw}(\lambda)$.

Based on the aforementioned analysis, it can be expected that the water-leaving radiance from the shadowed pixel $(L_w^{sdw}(\lambda))$ reaching the satellite sensor is lower than the water-leaving radiance from the neighboring sunlit pixels $(L_w^{sny}(\lambda))$. Here, we are assuming that the optical properties of the water in the two regions are the same since they are adjacent. Also, the path radiance from the shadowed pixel is slightly lower since part of the atmosphere is also shadowed. A shadowed portion of the atmosphere must produce less path radiance, depending on how much of the atmosphere is shadowed, while we are assuming that the atmosphere is nearly uniform. Thus, the total radiance measured over the shadowed pixel is lower than that measured over the neighboring sunlit pixel. The uncalibrated raw digital counts of the shadowed pixel will also be lower than those of the neighboring sunlit pixel since they are adjacent and the sunlit region is brighter. An example of this is shown in Fig. 1(c), where the red spectra represent $L_t^{sdw}(\lambda)$ and the green spectra represent the adjacent $L_t^{sny}(\lambda)$ taken from a HICO image acquired over Guam Island on November 11, 2009. It can be seen clearly that the adjacent sunlit pixel has higher digital counts (green spectra) than the shadowed pixel (red spectra) due to the differences in illuminations.

IV. DEVELOPMENT OF THE CSDI

Although the spectral radiance amplitude of the shadowed region is slightly lower than that of the neighboring sunlit region, this difference is relatively small. Furthermore, because of different path radiances and water-leaving radiances, the measured radiance from some other sunlit region may be exactly the same with or sometimes even lower than the radiance of the shadowed spectra [see Fig. 1(c)]. This indicates that the spectral shape or amplitude alone is not adequate to separate the two
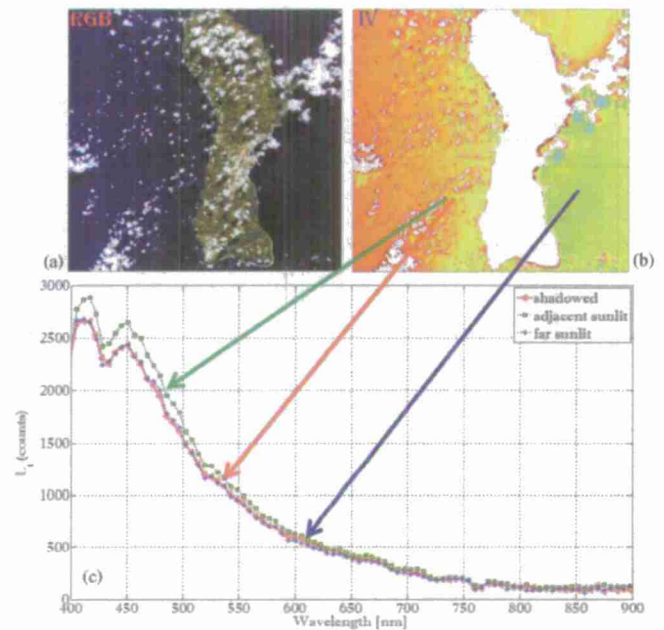

Fig. 1. (Top left) (a) HICO true color image (November 11, 2009) over Guam. (Top right) (b) Corresponding IV image, where clouds and lands are shown in white and the shadowed regions are shown in slightly cooler color compared to the surrounding sunlit regions. (Bottom) (c) Top-of-the-atmosphere radiance spectra from (red) shadowed, (green) adjacent sunlit, and (blue) far sunlit regions. The red, green, and blue arrows show the locations of the radiance spectra of the shadowed, adjacent sunlit, and far sunlit pixels, respectively, on the IV image. The spectrum from the shadowed pixel is very similar to the spectrum from the far sunlit pixel. Sometimes, the shadowed spectrum can even be higher than the spectrum from some other sunlit regions. This indicates that spectral profile alone is not adequate to separate the shadowed regions for an entire image.

regions for an entire image. However, the spectral amplitude can help us separate the two regions if a small portion of the image is examined at a time. The proposed shadow detection technique works in two steps. First, it amplifies the contrast between the shadowed and neighboring sunlit regions by taking advantage of the small differences in the spectral amplitudes, particularly in the blue–green region of the spectra [Fig. 1(c)]. To amplify the contrast of the two regions, we introduce an index called the Integrated Value (IV), which is defined as

$$IV = \int_{400 \text{ nm}}^{600 \text{ nm}} Lt(\lambda)d\lambda. \quad (3)$$

Even though the IV index allows visual separation of the two regions to an observer, IV itself is not adequate to separate based on a threshold. This is because the IV index from a shadowed region can be very close to, or even higher than, the IV index of some other sunlit region. This can be seen in the IV image in Fig. 1(b), where clouds and lands are shown in white while shadows are shown in slightly cooler color compared to the neighboring sunlit regions.

To separate the shadowed and sunlit pixels using a constant threshold, we normalize the IV index of the pixel under investigation, by the mean of the IV indices within a spatial adaptive sliding box (ASB) centered on this pixel. This is the second step of our technique, where we examine small portion (the ASB) of the image at a time and normalize the image adaptively. The

adaptive normalization allows us to use a constant threshold for the entire image to separate the two regions. The selection of ASB size is explained after (4).

Based on the optical characteristics of the water and atmosphere in the shadowed and neighboring sunlit regions, we define a cloud shadow-detection technique called the CSDI as

$$CSDI = \frac{IV_c}{\langle IV_{\text{ASB}} \rangle} \qquad (4)$$

where IV_c represents the IV index of the pixel (the central pixel of the ASB) which needs to be classified as a shadowed or sunlit pixel. The $\langle IV_{\text{ASB}} \rangle$ represents the spatial mean of the IV indices within the selected ASB of this pixel. This process should be repeated for all pixels that need to be classified as shadowed or sunlit pixel. Note that, before applying the CSDI, cloud needs to be removed properly or spurious results can be expected since homogeneity within the ASB will not hold true. Additionally, the CSDI might break down in turbid coastal waters since water or even the atmosphere may not be homogeneous within the ASB. Thus, the CSDI is mainly for deep waters, where atmospheric and marine optical properties can be assumed homogeneous within the ASB.

The ASB needs to be selected carefully so that it only contains shadowed and sunlit pixels or only sunlit pixels. This is because the goal here is to make the denominator of CSDI (4) larger than the numerator for the shadowed pixels and vice versa for the sunlit pixels. Since the water and atmosphere are homogeneous within the ASB, the IV indices of the sunlit pixels will be close to each other, and they would be much higher than the IV indices of the neighboring shadowed pixels. Thus, if the selected ASB contains only sunlit pixels and the pixel under examination is also a sunlit pixel, the CSDI value for this pixel would be around one since the mean of the ASB [denominator of (4)] and the IV index [numerator of (4)] would be about the same. If the ASB contains both shadowed and sunlit pixels and the pixel under examination is a sunlit pixel, the CSDI value will be greater than one since the mean of the ASB will be slightly lower than the IV index of the pixel under examination. On the other hand, if the pixel under examination happens to be a shadowed pixel, the CSDI value would be less than one since the IV index of this shadowed pixel would be smaller than the mean of the ASB. Now, if the ASB contains only shadowed pixels, it can be problematic since the CSDI value will be around one, like the case of only sunlit pixels. They will be classified as sunlit pixels if the CSDI threshold is put less than one. That is why it is important to select the ASB in such a way that it is bigger than the shadowed region. This can be achieved by using the cloud size information since cloud is generally larger than the shadow and relatively easy to detect, even when using simplistic brightness thresholds.

V. RESULTS AND DISCUSSION

The CSDI technique uses the top-of-atmosphere radiance measured in raw digital counts, which does not require converting the data to radiance units. This can be advantageous for sensors with low radiometric accuracy. For example, the Hyperion sensor has a radiometric accuracy of only $\pm 5\%$ in the measured L_t. Such uncertainty in the L_t may cause a 50% error

in L_w by the standard-atmospheric-correction approach even with a perfect atmospheric model [7]. Detecting cloud shadows from raw digital counts will enable us to correct for the atmosphere using the cloud shadow atmospheric correction [7] from raw digital counts. Hence, the imperfect radiometric accuracy of those sensors can be overcome [7]. Furthermore, the cloud shadow atmospheric correction can also be automated [37].

The CSDI images were created using different ASBs (32 × 32 to 128 × 128) and the raw digital counts of the selected HICO images. Various thresholds were tested to separate the shadowed regions for multiple images. Separated shadowed regions were then visually compared with the corresponding true color and IV images. We used the true color and the IV images as the ground truth since shadows can be seen in both visually and, also, no other optical method is available to identify shadows over water. The IV image, however, is superior over the true color image since it integrates the spectra from 400 to 600 nm for each pixel. Because of the integration, the small differences in the spectral amplitudes between the two regions add up, amplifying the contrast significantly. For example, HICO has 35 channels in this spectral range. Thus, the HICO IV image shows a shadowed region that is much better than the corresponding true color image which only uses three channels. We compare the CSDI images with the corresponding true color and IV images. Our visual inspection shows that $CSDI <= 0.95$ is too low to detect relatively thin part of the shadows while $CSDI => 0.97$ is a little high and gives a false signal (a false signal increases with increasing CSDI threshold values). An example is shown in Fig. 2 (September 26, 2010, HICO image acquired over Pagan Island; an image size of 285 × 400 pixels; 128 × 128 ASB), where the IV image [Fig. 2(a)] is assumed to represent the true shadowed regions. A false shadowed region is detected [red circle in Fig. 2(d)] when CSDI is set as $<= 0.97$, with the error rectified when CSDI is set as $<= 0.96$ [Fig. 2(c)]. However, it can also be seen in the black-circled region that the $CSDI <= 0.97$ detects thin shadows or shadow edge pixels slightly better than $CSDI <= 0.96$. On the other hand, $CSDI <= 0.95$ is too low to detect relatively thin part of the shadows. The green circle shows a region where $CSDI <= 0.95$ [Fig. 2(b)] fails to detect part of the shadow while $CSDI <= 0.96$ or $CSDI <= 0.97$ detects it. Our visual inspection of a group of images shows that the overall performance of $CSDI <= 0.96$ is the optimal setting to minimize false signals while maximizing shadow region detection on HICO images. The threshold may need to be tuned for other hyperspectral or multispectral sensors.

As mentioned before, the clouds need to be removed before applying the CSDI. A band ratio between HICO band 35 (548 nm) and band 70 (748 nm) was used to flag the clouds. Using the proposed threshold ($CSDI <= 0.96$), an analysis of the ASB size was performed on the selected HICO images. The result is shown in Fig. 3, where the horizontal axis represents the ASB sizes (8 represents 8 × 8, 16 represents 16 × 16, 32 represents 32 × 32, 64 represents 64 × 64, and 128 represents 128 × 128 pixels) and the vertical axis represents the total percentage of the shadowed pixels in each image detected with different ASBs. These data were collected around the Virgin Islands on December 20, 2009, around Samoa on October 2, 2010, around Guam on November 11, 2009, and around
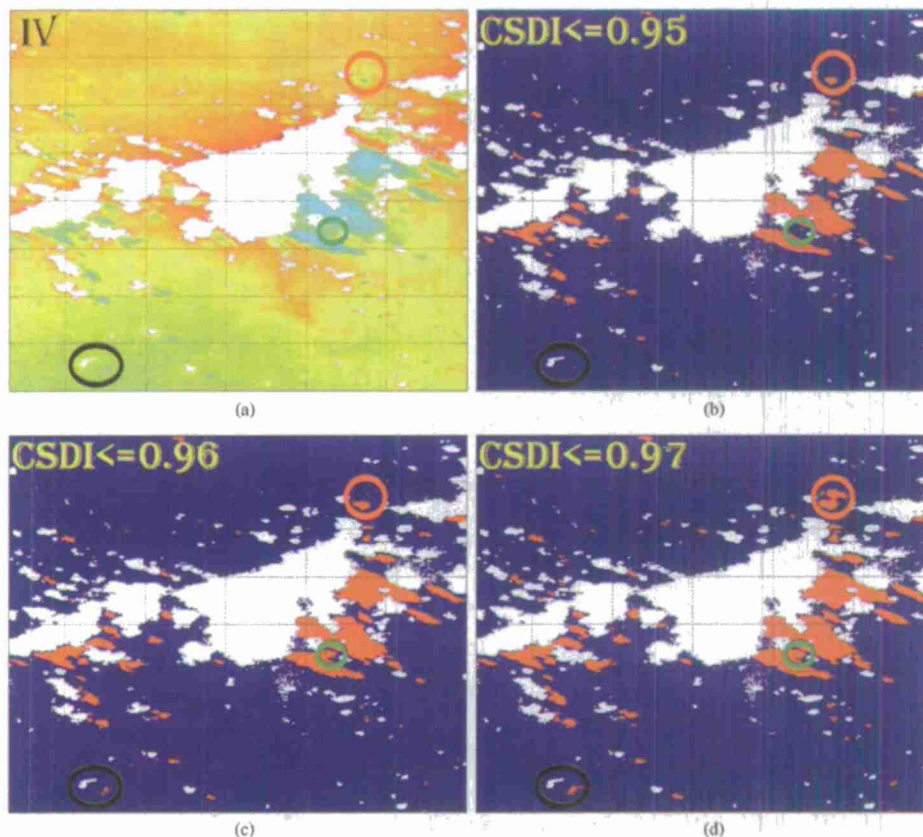
Fig. 2.　HICO image acquired over Pagan Island on September 26, 2010. (a) IV image (an image size of 285×400 pixels) where clouds are shown in white while the shadows are shown in slightly cooler color compared to the surrounding sunlit regions. Images (b), (c), and (d) are the corresponding CSDI images (created using a constant 128×128 ASB) with different CSDI thresholds ($CSDI <= 0.95$, $CSDI <= 0.96$, and $CSDI <= 0.97$, respectively), where clouds are shown in white, sunlit regions are shown in blue, and the shadows are shown in red. The black circle shows a region where $CSDI <= 0.97$ performs a little bit better on thin shadow detection while the red circle shows a region where it gives a false signal. The green circle shows a region where $CSDI <= 0.95$ does not detect part of the shadow while $CSDI <= 0.96$ and $CSDI <= 0.97$ detect it. The overall performance of $CSDI <= 0.96$ is the optimal setting to minimize false signals while maximizing shadow region detection.
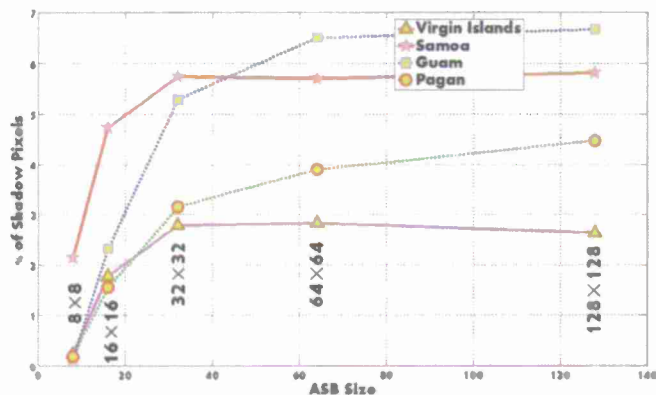

Fig. 3.　Size of the ASB versus the total percentage of the shadowed pixels in the images shown in Figs. 4 and 5. The (red and magenta) solid lines are for smaller shadows (from Fig. 4), while the (blue and green) dotted lines are for larger shadows (from Fig. 5). A 32×32 ASB appears to be adequate for the smaller shadows, but a larger ASB is required for the larger shadows. A larger ASB has little impact on the smaller shadow detection, as can be seen in the red and magenta lines which change little from 32×32 ASB to 128×128 ASB.

TABLE 1

PERCENTAGE OF PIXELS IDENTIFIED AS CLOUD, SHADOW, AND SUNLIT DUE TO DIFFERENT CLOUD MASKINGS FOR THE IMAGE SHOWN IN FIG. 2

Cloud masking	Percentage of shadow pixels	Percentage of sunlit pixels	Percentage of cloud pixels
Under	5.11	82.02	12.87
Proper	4.38	79.05	16.57
Over	2.52	65.36	32.12

Northern Mariana Pagan on September 26, 2010. Virgin Islands and Samoa have relatively smaller shadows, while Guam and Pagan have relatively larger shadows. It is obvious in Fig. 2 that 8×8 and 16×16 ASBs are too small to detect most of the shadowed pixels. A 32×32 ASB appears to be reasonable for the smaller shadows (Virgin Islands and Samoa), while a larger ASB is required for the larger shadows (Guam and Pagan). Visual inspection of the CSDI images with the corresponding true color and IV images shows that the shadowed pixels detected even with smaller ASBs such as 8×8 or 16×16 are in fact from the true shadowed regions. However, smaller ASBs only detect smaller portions of the shadows. On the other hand, larger ASBs have little impact on smaller shadows, as can be seen in Fig. 3 (red and magenta lines), where the percentage of the total shadowed pixels in the images does not change significantly from ASB size ranging from 32×32 to 128×128. Therefore, it might be advantageous to employ a large constant ASB based on the largest cloud size of an image and use that constant ASB for the entire image rather than an adaptive one that is based on regions of the image.
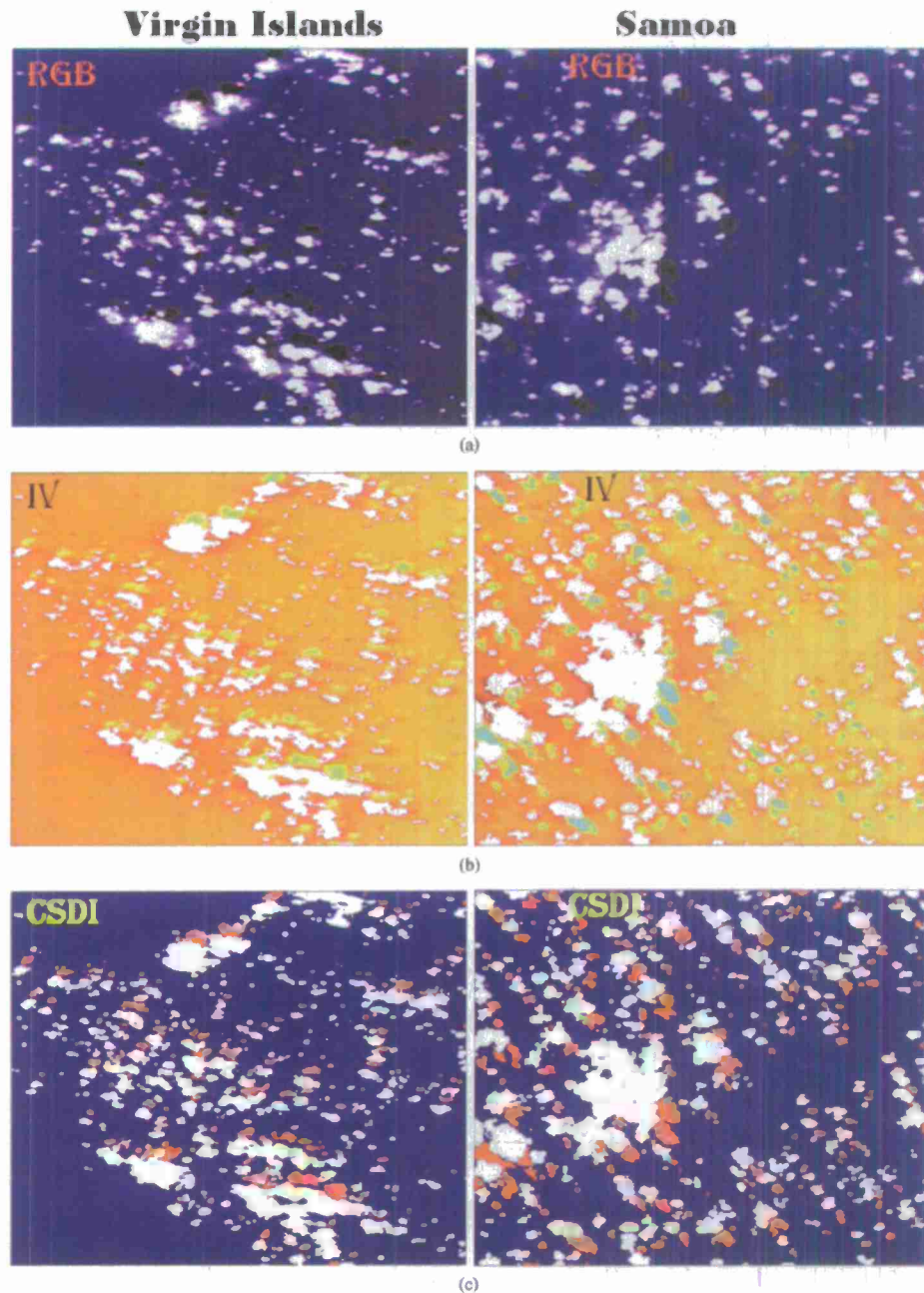
Fig. 4. Examples of relatively smaller cloud shadow detection using the CSDI technique. (Left panel) HICO image acquired over Virgin Islands on December 20, 2009 (an image size of 270 × 400 pixels). (a) True color image. (b) Corresponding IV image. (c) Corresponding CSDI image. (Right panel) HICO image acquired over Samoa on October 2, 2010 (an image size of 260 × 260 pixels). (d) True color image. (e) Corresponding IV image. (f) Corresponding CSDI Image. The clouds are shown in white on both CSDI and IV images, the shadows are shown in red on the CSDI images and in slightly cooler color on the IV image, and the sunlit regions are shown in blue on the CSDI images and in warmer color on the IV images. The true color, IV, and CSDI images agree pretty well. The cloud shadows are clearly seen in red structures adjacent to the white clouds on the CSDI images. The shape of the cloud shadow particularly for the isolated cloud closely follows that of the cloud, as expected.

Proper cloud masking is necessary for the CSDI approach to perform well. Table I shows the impact of the cloud masking on the image shown in Fig. 2. This analysis was performed using the proposed CSDI threshold (CSDI $<= 0.96$) and a 128 × 128 ASB since these two parameters gave the best results. A band ratio between HICO band 35 (548 nm) and band 70 (748 nm) was used for the cloud masking where the ratio less than or equal to 3 masks the cloud properly while 2.8 and 3.2 undermasks and overmasks the cloud, respectively. When cloud is masked properly, the detected shadow and sunlit regions agree very well with the corresponding red green blue and IV images. However, when cloud is undermasked, homogeneity within the ASB does not hold true around cloud regions since unmasked cloud has significantly higher radiance than the sunlit or shadow pixels. Thus, false results can be expected, as can be seen in Table I, where true shadow pixels are 4.38% of the total pixels but, because of the undermasking of the cloud, 5.11% of the pixels are identified as shadowed pixels. On the other hand,
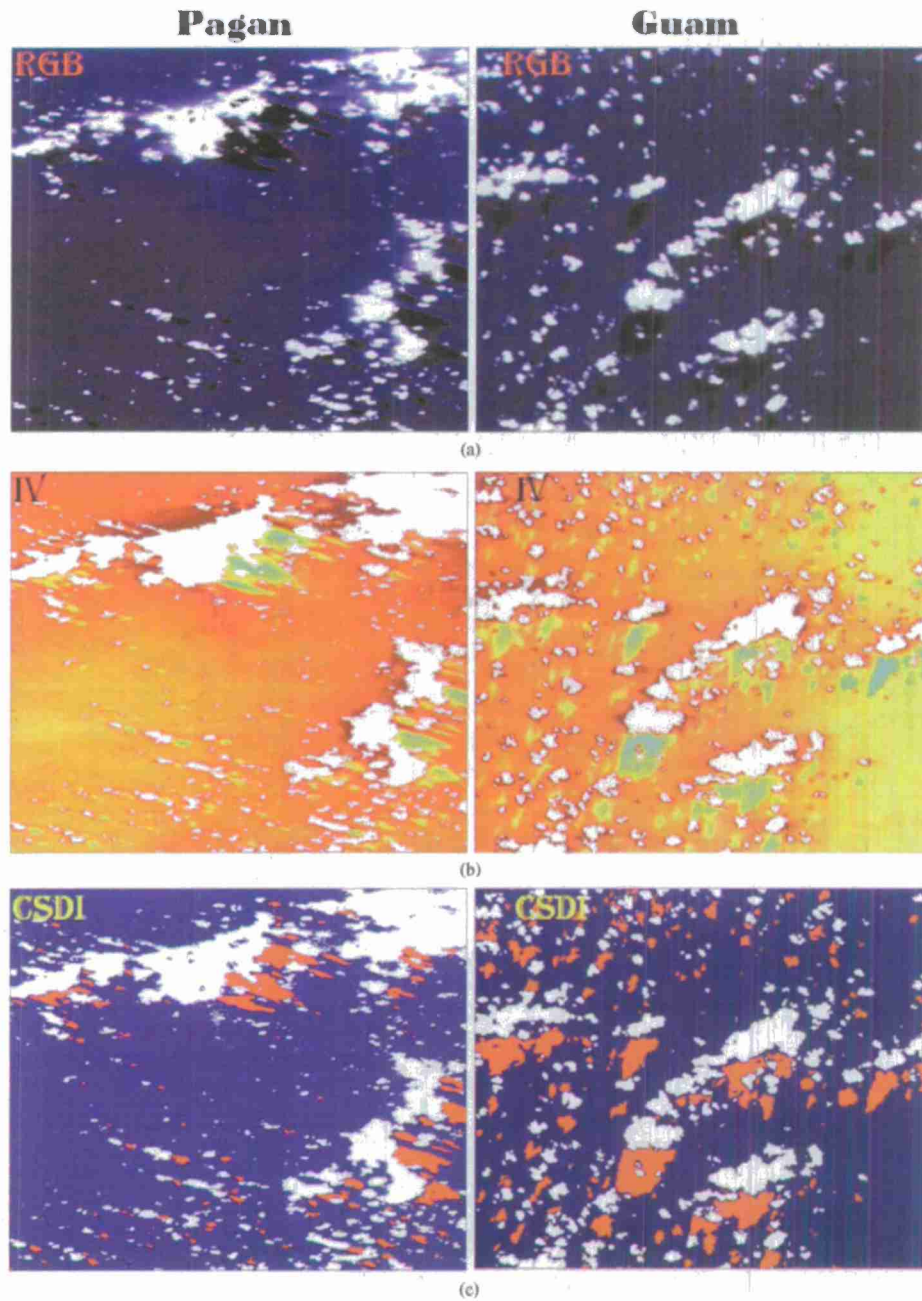
Fig. 5. Examples of relatively larger cloud shadow detection using the CSDI technique. (Left panel) HICO image acquired over Pagan on September 26, 2010 (an image size of 380 × 635 pixels). (a) True color image. (b) Corresponding IV image. (c) Corresponding CSDI image. (Right panel) HICO image acquired over Guam on November 11, 2009 (an image size of 275 × 275 pixels). (d) True color image. (e) Corresponding IV image. (f) Corresponding CSDI image. The clouds are shown in white on both CSDI and IV images, the shadows are shown in red on the CSDI images and in slightly cooler color on the IV images, and the sunny regions are shown in blue on the CSDI image and in slightly warmer color on the IV images. The true color, IV, and CSDI images agree pretty well. The cloud shadows are clearly seen in red structures adjacent to the white clouds on the CSDI images. The shape of the cloud shadow particularly for the isolated cloud closely follows that of the cloud, as expected.

if cloud is overmasked, CSDI identifies only 2.52% of the pixels as shadowed pixels. This is because the rest of the shadowed pixels are removed with the cloud masking. However, those 2.52% pixels are from the true shadow region. There is no false detection with the overmasking of the cloud, unlike the undermasking, but only portions of the shadows are detected. This is because homogeneity within the ASB remains true with overmasking of the cloud.

Examples of shadow detection with the CSDI method are shown in Figs. 4 and 5. Since larger ASBs have little impact on smaller shadows and works better for larger shadows, a 128 × 128 ASB was chosen for these images (Figs. 4 and 5). Fig. 4 (left panel) shows the HICO image acquired over Virgin Islands on December 20, 2009 (an image size of 270 × 400 pixels), where Fig. 4(a) shows the true color image, Fig. 4(b) shows the corresponding IV image, and Fig. 4(c)

shows the corresponding CSDI image. The right panel of Fig. 4 is another HICO image acquired over Samoa on October 2, 2010 (an image size of 260 × 260 pixels), where Fig. 4(d) shows the true color image, Fig. 4(e) shows the corresponding IV image, and Fig. 4(f) shows the corresponding CSDI image. Similarly, Fig. 5 left panel shows a HICO image acquired over Pagan on September 26, 2010 (an image size of 380 × 635 pixels), where Fig. 5(a) shows the true color image, Fig. 5(b) shows the corresponding IV image, and Fig. 5(c) shows the corresponding CSDI image. The right panel of Fig. 5 shows one more HICO image acquired over Guam on November 11, 2009 (an image size of 275 × 275 pixels), where Fig. 5(d) shows the true color image, Fig. 5(e) shows the corresponding IV image, and Fig. 5(f) shows the corresponding CSDI image. The clouds are shown in white on both CSDI and IV images, while the shadows are shown in red on the CSDI images and in slightly cooler color compared to the neighboring sunlit region on the IV images. The sunlit regions are shown in blue on the CSDI images and in slightly warmer color compared to the adjacent shadowed regions on the IV images. The true color, IV, and CSDI images agree reasonably well in both Figs. 4 and 5. The cloud shadows are clearly seen in red structures adjacent to the white clouds on the CSDI images. Also, the shape of the cloud shadow particularly for the isolated cloud closely follows that of the cloud, as expected, which reconfirms the potential of the CSDI method.

The CSDI method has several advantages over geometry-based [25], [26] or reflectance-threshold-based techniques [16]. It docs not require any thermal or short-wave infrared channels which are not always present on ocean color sensors. The CSDI method is entirely based on visible channcls, the most important spectral region for ocean color studies, which always exist on ocean color sensors. Although angular (solar and viewing) information can be acquired from the satellite sensors, it is still a challenge to estimate cloud vertical height accurately from satellite sensors. Some sensors, such as the Moderate Resolution Imaging Spectroradiomcter, can estimate cloud vertical height; howevcr, they are not very reliable [33]. Nonetheless, most ocean color sensors do not have the capability to estimate cloud vertical heights. Thus, a geometry-based approach is not appropriate for these sensors. On the other hand, the CSDI method does not require any estimation of cloud vertical heights or even any angular information. It is based on the top-of-the-atmosphere readings of the spaceborne or airborne sensors. Since it is based on the true measurement without any estimation, the dctected shadow locations are more precise. Furthermore, the CSDI is relatively easy to use and should be faster than the geometry-based approach since it requires less computation. Moreover, since the CSDI method uses the top-of-atmosphere radiance measured in raw digital counts, the method will still work well even with the sensors with high radiometric calibration errors, unlike the reflectance-threshold-based methods [16].

The CSDI cloud shadow-detection approach has some drawbacks. It cannot detect shadows in the edge pixels of the acquired satellite images, since an ASB cannot be selected centered on these pixels. However, an observer can use the IV image to visually identify the shadows in those pixels, since

shadow pixels appear slightly dimmer in the IV image than the neighboring sunlit pixels, as can be seen in Fig. 4(b) and (e) and Fig. 5(b) and (e). The CSDI may also give spurious results in nonhomogeneous turbid or shallow waters, since nonhomogeneity within the ASB may increase or decrease the mean values [denominator of (4)]. Thus, the CSDI method is not intended for use in nonhomogeneous waters. However, like the edge pixels, the IV image can be used to visually identify the shadow regions in those waters.

VI. CONCLUSION

A cloud shadow-detcction technique (CSDI) has been developed and applied to HICO data collected from various locations to isolate shadowed pixels. The shapes of the clouds and cloud shadows observed in the CSDI images closely resemble those of clouds and cloud shadows in the corresponding true color and IV images. The agreement between the true color, IV, and CSDI images is very reasonable over open ocean. This suggests the potential of the cloud shadow detection using the proposed technique which only uses the top-of-the-atmosphere optical readings of the spaceborne or airborne imagers. Although the proposed CSDI threshold works reasonably well on the selected HICO images, further studies are necessary to fine tune the threshold and the selection of optimal ASB size based on image scene content for automated processing.

REFERENCES

[1] A. S. Belward and C. R. Valenzuela, *Remote Sensing and Geographical Information System for Resource Management in Developing Countries*. Boston, MA: Kluwer, 1991.

[2] P. M. Dare, "Shadow analysis in high-resolution satellite imagery of urban areas," *Photogramm. Eng. Remote Sens.*, vol. 71, no. 2, pp. 169–177, 2005.

[3] J. J. Simpson and J. R. Stitt, "A procedure for the detection and removal of cloud shadow from AVHRR data over land," *IEEE Trans. Geosci. Remote Sens.*, vol. 36, no. 3, pp. 880–897, May 1998.

[4] R. Amin, J. Zhou, A. Gilerson, B. Gross, F. Moshary, and S. Ahmed, "Novel optical techniques for detecting and classifying toxic dinoflagellate *Karenia brevis* blooms using satellite imagery," *Opt. Exp.*, vol. 17, no. 11, pp. 9126–9144, May 2009.

[5] R. Amin, A. Gilerson, J. Zhou, B. Gross, F. Moshary, and S. Ahmed, "Impacts of atmospheric corrections on algal bloom detection techniques," in *Proc. 89th AMS Annu. Meeting*, Phoenix, AZ, Jan. 11–15, 2008.

[6] K. L. Carder, P. Reinersman, and R. F. Chen, "AVIRIS calibration using the cloud shadow method," in *Proc. Summ. 4th Annu. JPL Airborne Geosci. Workshop*, R. O. Green, Ed., 1992, vol. 1, pp. 26–28, JPL Publication 92-14.

[7] Z. P. Lee, B. Casey, R. Arnone, A. Weidemann, R. Parsons, M. J. Montes, B. Gao, W. Goode, C. O. Davis, and J. Dye, "Water and bottom properties of a coastal environment derived from Hyperion data measured from the EO-1 spacecraft platform," *J. Appl. Remote Sens.*, vol. 1, p. 011502, 2007.

[8] P. Reinersman, K. L. Carder, and F. R. Chen, "Satellite-sensor calibration verification with the cloud shadow method," *Appl. Opt.*, vol. 37, no. 24, pp. 5541–5549, Aug. 1998.

[9] R. T. McNider, J. A. Song, and S. Q. Kidder, "Assimilation of GOES-derived solar insolation into a mesoscale model for studies of cloud shading effects," *Int. J. Remote Sens.*, vol. 16, no. 12, pp. 2207–2231, 1995.

[10] A. Lipton, "Cloud shading retrieval and assimilation in a satellite-model coupled mesoscale analysis system," *Mon. Wea. Rev.*, vol. 121, no. 11, pp. 3062–3081, 1993.

[11] C. M. Gurney, "The use of contextual information to detect cumulus clouds and cloud shadows in Landsat data," *Int. J. Remote Sens.*, vol. 3, no. 1, pp. 51–62, 1982.

[12] T. Berendes, S. K. Sengupta, R. M. Welch, B. A. Wielicki, and M. Navar, "Cumulus cloud base height estimation from high spatial resolution

Landsat data: A Hough transform approach," *IEEE Trans. Geosci. Remote Sens.*, vol. 30, no. 3, pp. 430–443, May 1992.

[13] J. J. Simpson, T. McIntire, Z. Jin, and J. R. Stitt, "Improved cloud height estimation under arbitrary viewing and illumination conditions using AVHRR data," *Remote Sens. Environ.*, vol. 72, no. 1, pp. 95–110, Apr. 2000.

[14] J. Cihlar and J. Howarth, "Detection and removal of cloud contamination from AVHRR images," *IEEE Trans. Geos. Remote Sens.*, vol. 32, no. 3, pp. 583–589, May 1994.

[15] K. V. Khlopenkov and A. P. Trishchenko, "SPARC: New cloud, snow, cloud shadow detection scheme for historical 1-km AVHHR data over Canada," *J. Atmos. Ocean. Technol.*, vol. 24, no. 3, pp. 322–343, Mar. 2007.

[16] S. A. Ackerman, K. I. Strabala, P. Menzel, R. A. Frey, C. C. Moeller, and L. E. Gumley, "Discriminating clear sky from clouds with MODIS," *J. Geophys. Res.*, vol. 103, no. D24, pp. 32 141–32 157, Dec. 1998.

[17] W. B. Rossow and L. C. Garder, "Cloud detection using satellite measurements of infrared and visible radiances for ISCCP," *J. Clim.*, vol. 6, no. 12, pp. 2341–2369, 1993.

[18] S. Platnick, M. D. King, S. A. Ackerman, W. P. Menzel, B. A. Baum, J. C. Riedi, and R. A. Frey, "The MODIS cloud products: Algorithms and examples from Terra," *IEEE Trans. Geosci. Remote Sens.*, vol. 41, no. 2, pp. 459–473, Feb. 2003.

[19] M. Derrien, B. Farki, L. Harang, H. LeGleau, A. Noyalet, D. Pochic, and A. Sairouni, "Automatic cloud detection applied to NOAA-11/ AVHRR imagery," *Remote Sens. Environ.*, vol. 46, no. 3, pp. 246–267, Dec. 1993.

[20] J. F. Cayula and P. Cornillon, "Cloud detection from a sequence of SST images," *Remote Sens. Environ.*, vol. 55, no. 1, pp. 80–88, 1996.

[21] R. T. Pinker, X. Li, W. Meng, and E. A. Yegorova, "Toward improved satellite estimates of short-wave radiative fluxes—Focus on cloud detection over snow: 2. Results," *J. Geophys. Res.*, vol. 112, p. D09204, 2007. doi:10.1029/2005JD006699.

[22] G. Wind, S. Plantnick, M. D. King, P. A. Hubanks, M. J. Pavolonis, A. K. Heidinger, P. Yang, and B. A. Baum, "Multilayer cloud detection with the MODIS near-infrared water vapor absorption band," *J. Appl. Meteorol. Clim.*, vol. 49, no. 11, pp. 2315–2333, Nov. 2010.

[23] P. Y. Chen, R. Srinivasan, G. Fedosejevs, and B. Narasimhan, "An automated cloud detection method for daily NOAA-14 AVHRR data for Texas, USA," *Int. J. Remote Sens.*, vol. 23, no. 15, pp. 2939–2950, 2002.

[24] B. Wang and A. Ono, "Automated detection and removal of clouds and their shadows from Landsat TM images," *IEICE Trans. Inf. Syst.*, vol. E82-D, no. 2, pp. 453–460, Feb. 1999.

[25] J. J. Simpson, Z. Jin, and J. R. Stitt, "Cloud shadow detection under arbitrary viewing and illumination conditions," *IEEE Trans. Geosci. Remote Sens.*, vol. 38, no. 2, pp. 972–976, Mar. 2000.

[26] K. D. Hutchison, R. L. Mahoney, E. F. Vermote, T. J. Kopp, J. M. Jackson, A. Sei, and B. D. Iisager, "A geometry-based approach to identifying cloud shadows in the VIIRS cloud mask algorithm for NPOESS," *J. Atmos. Ocean. Technol.*, vol. 26, no. 7, pp. 1388–1397, Jul. 2009.

[27] J. Liu, T. Fang, and D. Li, "Shadow detection in remotely sensed images based on self-adaptive feature selection," *IEEE Trans. Geosci. Remote Sens.*, vol. 49, no. 12, pp. 5092–5103, Dec. 2011.

[28] A. Makarau, R. Richter, R. Muller, and P. Reinartz, "Adaptive shadow detection using a blackbody radiator model," *IEEE Trans. Geosci. Remote Sens.*, vol. 49, no. 6, pp. 2049–2059, Jun. 2011.

[29] K. Chung, Y. Lin, and Y. Huang, "Efficient shadow detection of color aerial images based on successive thresholding scheme," *IEEE Trans. Geosci. Remote Sens.*, vol. 47, no. 2, pp. 671–682, Feb. 2009.

[30] V. J. D. Tsai, "A comparative study on shadow compensation of color aerial images in invariant color models," *IEEE Trans. Geosci. Remote Sens.*, vol. 44, no. 6, pp. 1661–1671, Jun. 2006.

[31] S. A. Ackerman, K. I. Strabala, P. Menzel, R. A. Frey, C. C. Moeller, L. E. Gumley, B. Baum, S. W. Seemann, and H. Zhang, *Discriminating Clear-Sky From Clouds With MODIS Algorithm Theoretical Basis Document*. Madison, WI: Coop. Inst. Meteorol. Satell. Stud., 2006, p. 129, MOD35 verion 5.0.

[32] G. L. Stephens, D. G. Vane, R. J. Boain, G. G. Mace, K. Sassen, Z. Wang, A. J. Illingworth, E. J. O'Connor, W. B. Rossow, S. L. Durden, S. D. Miller, R. T. Austin, A. Benedetti, and C. Mitrescu, "The CloudSat mission and the A-train: A new dimension of space-based observations of clouds and precipitation," *Bull. Amer. Meteorol. Soc.*, vol. 83, pp. 1771–1790, 2002.

[33] Y. Luo, A. P. Trishchenko, and K. V. Khlopenkov, "Developing clear-sky, cloud and cloud shadow mask for producing clear-sky composites at 250-meter spatial resolution for the seven MODIS land bands over Canada and North America," *Remote Sens. Environ.*, vol. 112, no. 12, pp. 4167–4185, 2008.

[34] R. Richter and A. Muller, "De-shadowing of satellite/airborne imagery," *Int. J. Remote Sens.*, vol. 26, no. 15, pp. 3137–3148, 2005.

[35] M. D. Lewis, R. W. Gould, R. A. Arnone, P. E. Lyon, P. M. Martinolich, R. Vaughan, A. Lawson, T. Scardino, W. Hou, W. Snyder, R. Lucke, M. Carson, M. Montes, and C. Davis, "The Hyperspectral Imager for the Coastal Ocean (HICO): Sensor and data processing overview," in *Proc. IEEE Oceans*, Biloxi, MS, Oct. 26–29, 2009, pp. 1–9.

[36] R. L. Lucke, M. Corson, N. R. McGlothlin, S. D. Butcher, D. L. Wood, D. R. Korwan, R. R. Li, W. A. Snyder, C. O. Davis, and D. T. Chen, "The Hyperspectral Imager for the Coastal Ocean (HICO): Instrument description and first images," *Appl. Opt.*, vol. 50, no. 11, pp. 1501–1516, Apr. 2011.

[37] R. Amin, R. Gould, W. Hou, Z. Lee, and R. Arnone, "Automated detection and removal of cloud shadows on HICO images," in *Proc. SPIE Defense, Secur. Sens.*, Orlando, FL, Apr. 26–27, 2011.

Ruhul Amin was born in Sylhet, Bangladesh. He received the B.E. degree in computer engineering and the M.E. degree in electrical engineering from The City College of New York, New York, in 2005 and 2008, respectively, and the M.Phil. and Ph.D. degrees in electrical engineering from The City University of New York, New York, both in 2008 and 2009, respectively.

Since 2009, he has been a Research Scientist with the U.S. Naval Research Laboratory, Stennis Space Center, MS. He has developed optical algorithms to detect and classify harmful algal blooms from space. His current research interests include optical algorithm development, atmospheric corrections, cloud shadows, fluorescence, and harmful algal blooms.

Richard Gould received the B.S. degree (Oceanography, Biological Section) from Florida Institute of Technology, Melbourne, in 1981 and the Ph.D. degree (Oceanography, Biological Section) from Texas A&M University, College Station, in 1987.

He has over 25 years of oceanographic experience in phytoplankton ecology/systematics and ocean color remote sensing. He has developed and validated new multispectral and hyperspectral coastal ocean color algorithms, and he has transitioned satellite products to both the U.S. Navy and National Aeronautics and Space Administration. He is currently with the U.S. Naval Research Laboratory, Stennis Space Center, MS, where he manages the Bio-Optical/Physical Processes and Remote Sensing Section. His current research interests include satellite algorithm development, uncertainty analyses, optical water mass classification, coastal hypoxia, surface/subsurface linkages, and physical/bio-optical coupling.

Weilin "Will" Hou received the Ph.D. degree from the University of South Florida, Tampa, in 1997.

He is currently an Oceanographer with the U.S. Naval Research Laboratory, Stennis Space Center, MS, where he manages the Hydro Optics Sensors and Systems Section. His research interests include ocean optics, underwater imaging, optical turbulence, remote sensing including light detection and ranging, numerical simulation, data management, instrumentation, and platforms including unmanned aerial and underwater vehicles.

Dr. Hou is the Editor of the *Proceedings of the Society of Photo-Optical Instrumentation Engineers* (SPIE) Volumes 8372, 8030, 7678, and 7317. He helps SPIE organize the Ocean Sensing and Monitoring Conference as part of SPIE Defense and Security Symposium.

Robert Arnone received the B.S. degree in geology from Kent State University, Kent, in 1971 and the M.S. degree in geophysical sciences from the Georgia Institute of Technology, Atlanta, in 1974.

He is currently with the U.S. Naval Research Laboratory (NRL), Stennis Space Center, MS, where he leads the Ocean Processes Branch of over 40 scientists/technicians and staff of physical, biological, and optical and remote sensing ocean personnel specializing in coupled dynamic processes (biophysical modeling), mesoscale and fine-scale physical processes (marginal seas, wave dynamics, and coastal processes), remote sensing and ocean optics (naval electro optical systems, hyperspectral algorithms, and satellite applications), and marine molecular processes. He leads research in basic and exploratory research and applied oceanography for the U.S. Navy and federal agencies of the National Oceanic and Atmospheric Administration (NOAA) and National Aeronautics and Space Administration (NASA). He is currently leading the Ocean National Calibration/Validation efforts for the satellite ocean Joint Polar Satellite System for NASA, NOAA, and the U.S. Navy. He is coordinating the NRL hyperspectral satellite Hyperspectral Imaging of the Coastal Ocean, which was successfully launched to the International Space Station (in August 2009). He serves on the Science Teams for NASA, NOAA, the Environmental Protection Agency, and the U.S. Navy for developing future satellite systems and for establishing policy for ocean and coastal research. He has been an Adjunct Faculty Member with the Marine Science Department, The University of Southern Mississippi (USM), Hattiesburg, since 1989 and the University of South Alabama, and serves on graduate student committees (USM and Rosenstiel School of Marine and Atmospheric Sciences). He has developed bio-optical algorithms for satellites, which are applied to ecological forecasting models. He has received U.S. Department of Navy patents (1980). He has over 90 scientific publications and more than 250 presentations. His specific expertise is in coupling biological, optical, and physical processes using ocean color satellite and ocean models.

Mr. Arnone was the recipient of awards for naval honors for "science to operations" transitions and NRL Alan Berman publication awards. He has received NASA honors for astronaut training programs, U.S. Department of Navy honors, and NASA honors for Shuttle Astronaut Training program. He was also the recipient of the Navy Meritorious Civilian Service Award in 2008, U.S. Navy Employee of the Year in 1998, Navy Royalty Transition Award for Automated Processing in 2002, Naval Oceanographic and Atmospheric Research Laboratory Paper Award in 1992, and NRL's Alan Berman Award Division award for best paper in 1998, 2002, and 2008.

Zhongping Lee received B.S. degree in physics from Sichuan University, Chengdu, China, in 1984, the M.S. degree in physics from the Ocean University of China, Qingdao, China, and the Ph.D. degree from the University of South Florida (USF), Tampa, in 1994.

He stayed in USF as a Postdoctoral Researcher and a Research Associate after his graduation, joined the U.S Naval Research Laboratory in 2002, and is currently a professor in the Department of Environmental, Earth and Ocean Sciences, University of Massachusetts. He has conducted studies in both basic and applied aspects of ocean optics and ocean color remote sensing and published extensively on the fundamentals of ocean optics and algorithm developments for ocean color remote sensing.